Journal of *Marine Science and Engineering*

MDPI

Article

3D FE-Informed Laboratory Soil Testing for the Design of Offshore Wind Turbine Monopiles

Xiaoyang Cheng [1,*], Andrea Diambra [1], Erdin Ibraim [1], Haoyuan Liu [2] and Federico Pisanò [3]

[1] Department of Civil Engineering, University of Bristol, Bristol BS8 1QU, UK; Andrea.Diambra@bristol.ac.uk (A.D.); Erdin.Ibraim@bristol.ac.uk (E.I.)
[2] Department of Offshore Energy, Norwegian Geotechnical Institute (NGI), 0806 Oslo, Norway; haoyuan.liu@ngi.no
[3] Faculty of Civil Engineering and Geosciences, Delft University of Technology, Stevinweg 1, 2628 CN Delft, The Netherlands; F.Pisano@tudelft.nl
* Correspondence: Xiaoyang.Cheng@bristol.ac.uk

Abstract: Based on advanced 3D finite element modelling, this paper analyses the stress paths experienced by soil elements in the vicinity of a monopile foundation for offshore wind turbines subjected to cyclic loading with the aim of informing soil laboratory testing in support of monopile foundation design. It is shown that the soil elements in front of the laterally loaded monopile are subjected to complex stress variations, which gradually evolve towards steady stress cycles as the cyclic lateral pile loading proceeds. The amplitude, direction and average value of such steady stress cycles are dependent on the depth and radial distance from the pile of the soil element, but it also invariably involves the cyclic rotation of principal stress axes. Complementary laboratory testing using the hollow-cylinder torsional apparatus was carried out on granular soil samples imposing cyclic stress paths (with up to about 3×10^4 cycles) which resemble those determined after 3D finite element analysis. The importance of considering the cyclic rotation of principal stress axes when investigating the response of soil elements under stress conditions mimicking those around a monopile foundation subjected to cyclic lateral loading is emphasised.

Keywords: finite element analysis; soil; monopile; offshore; wind turbines; laboratory testing

Citation: Cheng, X.; Diambra, A.; Ibraim, E.; Liu, H.; Pisanò, F. 3D FE-Informed Laboratory Soil Testing for the Design of Offshore Wind Turbine Monopiles. *J. Mar. Sci. Eng.* **2021**, *9*, 101. https://doi.org/10.3390/jmse9010101

Received: 19 December 2020
Accepted: 14 January 2021
Published: 19 January 2021

1. Introduction

Renewable offshore wind energy has been playing a crucial role in meeting the increasing demand for green energy and reducing the global carbon footprint. In 2019, Europe installed a record of 3.6 GW of new offshore wind capacity, mostly located in the North Sea [1]. To date, with offshore wind turbines being installed mostly in shallow coastal waters, monopile foundation has been typically the preferred foundation option [1]. However, with the progressive increase of wind turbine capacity and the progressive research for additional and stronger wind resources in deeper water, the size of the monopile foundation has been progressively increasing in the last decade. It is currently conceivable to install monopiles with diameter in excess of 10 metres.

The increase in monopile foundation size is associated with an increased overall cost of the material as well as with the requirement of specialised vessels and installation equipment able to deal with the larger monopile sizes and weights. However, cost savings are necessary to ensure the long-term sustainability of wind farm developments if compared to other onshore energy resources. Therefore, engineers are not only facing the challenges of designing larger foundation under stricter and harsher environmental conditions, but they are also continuously asked to increase the cost-effectiveness of their design.

The recently proposed PISA (PIle Soil Analysis) design methodology (i.e., [2,3]) and its immediate uptake by the geotechnical offshore industry is the most obvious example of the design optimisation process within the geotechnical offshore discipline. The PISA

design methodology emphasises the importance of using advanced 3D finite element (FE) procedures to derive accurate soil reaction curves. These can then be implemented in a 1D finite element idealised monopile system, which becomes cost- and time-effective when analysing a large number of loading and limit state scenarios for individual wind turbines. Nevertheless, the accuracy of the 3D FE prediction is of paramount importance and it is well known that the choice of appropriate soil constitutive models and their calibration can severely affect the outcome of numerical FE analyses.

The current laboratory practice, to determine and calibrate constitutive soil parameters for the design of offshore wind monopile foundations, typically relies on cyclic triaxial and simple shear tests. Following the simplified analysis of the stress states discussed in Randolph and Houlsby [4], Fan and Long [5], Won et al. [6] and Ahmed and Hawlader [7], it can be assumed that cyclic triaxial conditions mimic the loading condition of a soil element in front of the laterally loaded pile while cyclic simple shear tests simulate the cyclic tangential shearing experienced by elements on the side of the pile. However, the stress state of soil surrounding a laterally loaded pile is more complex and rotation of principal stress axes within the soil around the pile invariably occur (i.e., [8]). Results from soil laboratory testing performed by Wichtmann et al. [9], Tong et al. [10] and Mandolini et al. [11] among others, have shown that the rotation of principal stress axes affects the overall soil response and the generation of plastic accumulated strains.

This paper shows how an advanced 3D finite element model can be used to investigate the stress paths induced by cyclic storm loading in different soil elements in front of a laterally loaded pile. The performed 3D finite element model employs the latest developments in cyclic soil constitutive modelling proposed by Liu et al. [12], which can accurately predict the expected soil response under a large number of loading cycles using the concept of hardening memory surface [13]. Informed by the cyclic stress paths extracted from the 3D FE analysis, complementary laboratory tests on granular soil samples have been conducted using the University of Bristol's hollow-cylinder torsional apparatus. It is shown that advanced laboratory tests, able to impose the cyclic rotation of principal stress axes, can provide a more representative characterisation of the mechanical response for elements located in front of cyclic laterally loaded monopile foundations.

2. 3D Finite Element Investigation

2.1. Numerical Modelling

The 3D FE model used in this study is representative of typical industry practice for an 8 MW-capacity wind turbine supported by a steel hollow monopile foundation driven in medium-dense/dense sand (relative density Dr = 50%). The dimensions of the monopile foundation follow those used by Kementzetzidis [14] and they are illustrated in Figure 1, featuring a monopile diameter (D) of 8.0 m, an embedded monopile length (L) of 27 m and a wall thickness (t) of 0.062 m. The FE model was set in the Opensees software [15], taking advantage of the geometrical symmetry of the problem as shown in Figure 1. The overall dimensions of the soil domain were 70 m $\times$ 35 m $\times$ 47 m to minimise the effect of the boundary conditions on the stress distribution in the soil nearby the monopile. The soil domain was represented with 12,024 eight-node hexahedral SSPbricks elements [16], which are effective against shear/volumetric locking issues in FE calculations. The same type of elements were adopted to simulate the underground section of the pile, which is modelled as a 3D hollow cylinder, featuring linear-elastic response represented by a Young's modulus, E = 200 GPa and Poisson's ratio, ν = 0.30. The aboveground part of the pile was modelled as an elastic beam by using 20 Timoshenko beam elements. The soil-pile interface was simulated according to Griffiths [17] by inserting a thin layer of solid elements, with a thickness equal to 4% of the monopile diameter along the shaft, 8% of the pile diameter under the tip. The elastic shear modulus and critical stress ratio were set to two or three and three or four times lower than those of the surrounding soil. The base of the model was fixed against movement in any direction. The lateral surfaces were restrained in the directions perpendicular to it. The ground surface was free to displace.

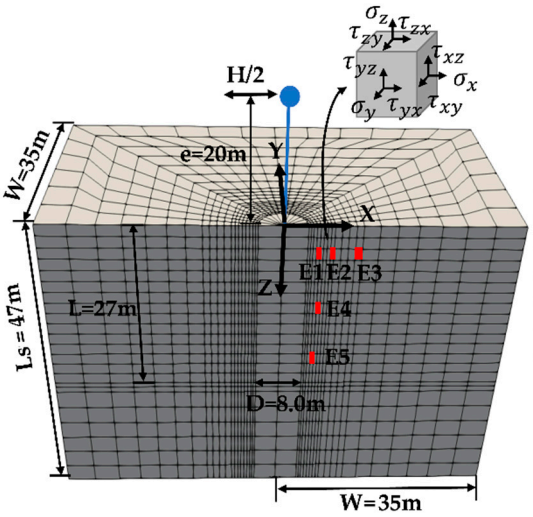

Node name	x/D	z/L
E1	0.65	0.15
E2	1	0.15
E3	1.35	0.15
E4	0.65	0.5
E5	0.65	0.85

Figure 1. Finite element model for monopile and investigated soil elements.

The soil behaviour was modelled using the enhanced version of the SANISAND04 (Simple ANIsotropic SAND) model [18] proposed by Liu et al. [12], named SANISAND-MS after the inclusion of an additional memory surface to capture the cyclic ratcheting behaviour of the soil under long-term cyclic loading. The adopted values of the constitutive parameters were aligned with those proposed by Dafalias et al. [18] for the original SANISAND04 parameters and by Liu et al. [12] for the memory surface related parameters in quartz sands, as summarised in Table 1.

Table 1. Values of parameters used in the memory surface constitutive model [12,18].

Parameter	Description	Value	Parameter	Description	Value
G_0	Dimensionless shear modulus	125	h_0	Hardening parameter	7.05
v	Poisson's ratio	0.3	c_h	Hardening parameter	0.968
M	Critical stress ratio	1.25	n^b	Void ratio dependence parameter	1.1
c	Compression to extension strength ratio	0.712	A_0	'Intrinsic' dilatancy parameter	0.704
e_0	Reference critical void ratio	0.934	n^d	Void ratio dependence parameter	3.5
λc	Critical state line shape parameter	0.02	μ_0	Ratcheting parameter	200
ξ	Critical state line shape parameter	0.7	ζ	Memory surface shrinkage parameter	0.0005
m	Yield locus opening parameter	0.01	β	Dilatancy memory parameter	1

The numerical analysis was carried out in three main stages: (1) the application of the geostatic pressure, (2) pile installation simulated as "wished in place", whose effect was not considered in this study (experimental and numerical assessments of the effect of

installation on monopile response can be found in the very recent studies by Fan et al. [19], Heins et al. [20] and Staubach et al. [21]), and (3) the application of the lateral cyclic loading at pile head located at a height, e, of 20 m above ground level. The cyclic lateral loading stage considered 80 one-way cycles with a total load amplitude of 10 MN (H in Figure 1) at the pile head applied in the form of a of sinusoidal load history. This corresponds to an applied maximum moment M_{max} equal to 40% of the monotonic lateral moment causing rotation of pile head equal to 0.5°, in line with the typical storm loading conditions as imposed in the experimental programme by Leblanc et al. [22].

The stress conditions induced by the cyclic lateral loading were inspected for five soil elements E1 to E5, as shown in Figure 1. Their horizontal distance and depth normalised by the pile diameter and length, respectively with respect to the origin of a cartesian reference system located at the centre of the pile and at the ground level, are also given in Figure 1. The adopted convention for the normal and shear stress components for each soil element follows the adopted cartesian reference system as also reported in Figure 1. It should be noted that in this simplified case, the soil was considered to be drained, with a dry unit weight γ_{dry} = 15.6 kN/m^3. Therefore, the stresses were all effective in this paper.

2.2. 3D FE Simulation Results

2.2.1. General Features of Cyclic Pile Response

The overall response of the monopile foundation is reported in Figure 2. The lateral force versus pile head displacement and the applied moment versus pile head rotation are reported in Figure 2a,c, respectively. The pile head displacements and rotation versus number of applied cycles are shown in Figure 2b,d, respectively. These plots show the capability of the FE model to predict the trends of progressive accumulation of displacement and rotation as observed in model pile tests [22,23]. Larger accumulations of rotation and displacements were observed at the early cyclic stages, followed by a progressive stiffening of the pile repose and a decrease in the rate of displacement and rotation accumulation. This response could be predicted owing to the capabilities of the employed constitutive model, which has proved to satisfactorily capture the ratcheting behaviour and the progressive soil stiffening under cyclic loading [12,24,25].

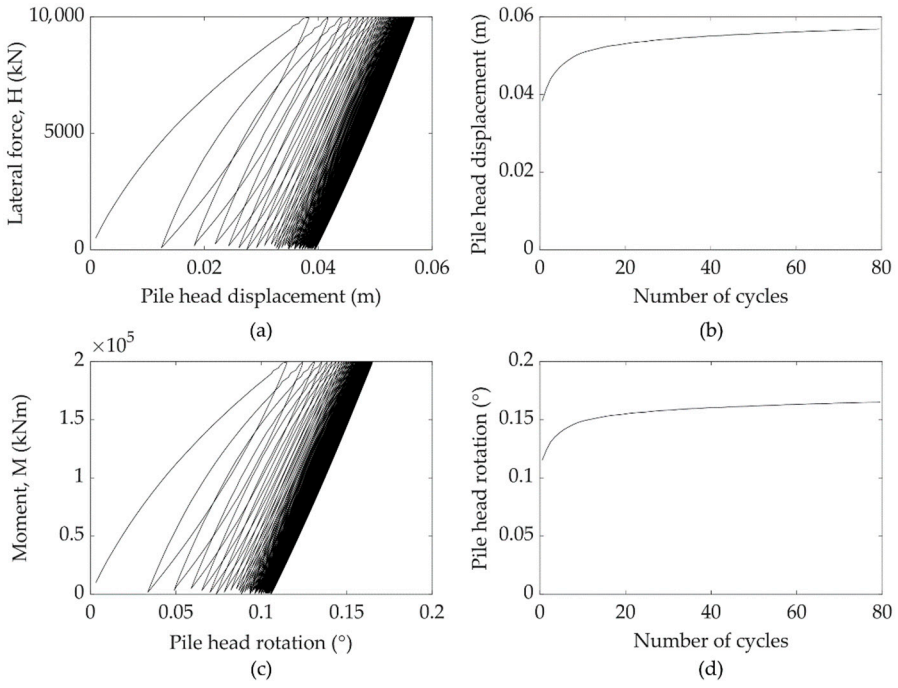

Figure 2. (**a**) Lateral load versus pile head displacement; (**b**) pile head displacement versus no. of cycles; (**c**) moment versus pile head rotation; (**d**) pile head rotation versus no. of cycles.

2.2.2. Stress Paths for the Investigated Soil Elements

The application of the cyclic lateral load may cause, for a given soil element, the variation of all six stress components. However, the inspection of the stress components variation for the investigated elements revealed that the two components of the shear stress (τ_{xy} and τ_{yz}) outside the x-z plane remained constant with a value close to zero for the applied cyclic loading, as shown in Figure 3 for the element E1. This observation is quite advantageous in the context of soil element laboratory testing in which the simultaneous control of the six stress components is unachievable by the current laboratory element testing capabilities. The hollow-cylinder torsional apparatus (HCTA) is the only experimental equipment permitting the simultaneous control of up to four stress components (but only one shear stress component). Therefore, considering the observed stress variation in Figure 3 and the practical limitation of testing practice, the analysis of the stress components for the selected soil elements is limited to those components in the x-z plane which is parallel to the direction of lateral loading (see Figure 4).

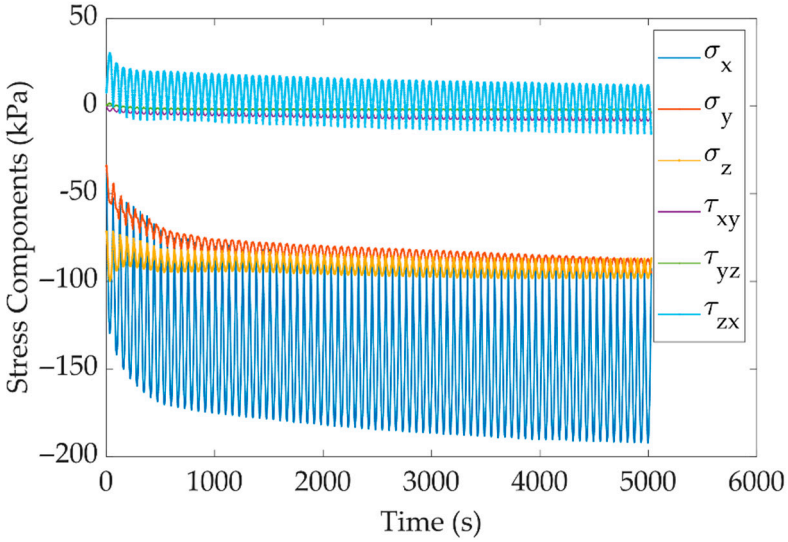

Figure 3. Variation of stress components during applied cyclic loading for element E1.

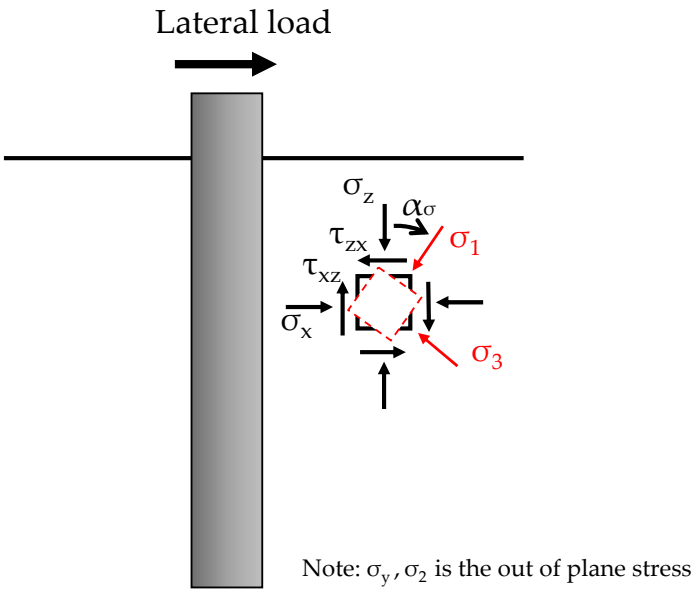

Figure 4. Considered stress components in the analysis.

The stress path from the FE analysis for the investigated soil element E1 is reported in Figure 5 in the τ_{xz}/p versus $(\sigma_x - \sigma_z)/2/p$ stress plane, where p is the mean isotropic stress, a conventional representation plane for hollow-cylinder torsional testing results [26]. For reference, Figure 5 also reports the Matsuoka–Nakai [27] peak failure envelope for the sand material for an assumed friction angle φ of 42°, which was the maximum mobilised friction angle observed in the FE simulations. The applicability of the Matsuoka–Nakai criterion for the material tested and the loading conditions was demonstrated by Mandolini et al. [28]. The initial stress for the element E1 lies on the negative side of the $(\sigma_x - \sigma_z)/2/p$ as a result of the vertical stress being higher than the horizontal. Application of the cyclic lateral pile loading induces an inclined stress path, which progressively moves towards the positive side of the $(\sigma_x - \sigma_z)/2/p$ as the cyclic loading proceeds but it also seems to evolute with a decreasing rate. The stress path corresponding to the last loading cycle is also singled out in Figure 5 and it is characterised by an inclination βc on the assumed stress plane. Such a stress path produces a rotation of principal stress axes (α_σ in Figure 4). It should be noted that, since a stress path imposed in a triaxial test would be represented by a horizontal stress path lying on the $(\sigma_x - \sigma_z)/2/p$, such conditions would not be simulated by triaxial tests.

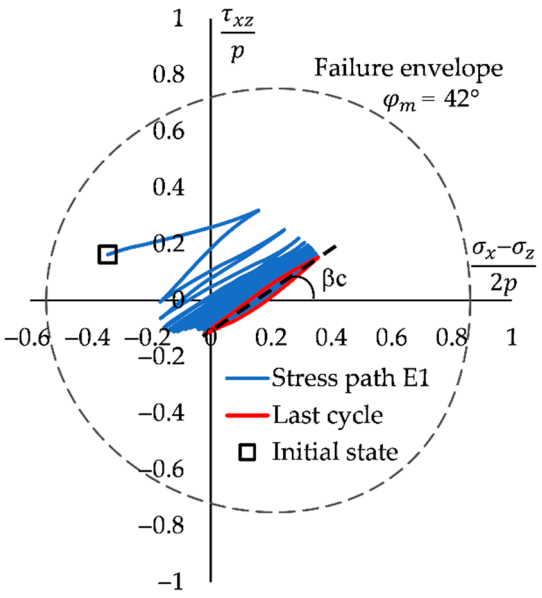

Figure 5. Stress path for element E1.

Figure 6 summarises the stress paths from FE analysis for all the investigated elements. Figure 6a reports the variation of the stress paths on elements E1, E2 and E3 located at the same depth (z/L = 0.15) but with different horizontal radial distances from the pile (x/D = 0.65, 1.0 and 1.35, respectively). The three elements start from a very similar normalised stress state but reach different final asymptotic stress cycles. As expected, the influence of the applied cyclic loading decreased with increasing distance from the pile, resulting in a lower amplitude of the cycle but also in a more limited transition towards the positive side of the $(\sigma_x - \sigma_z)/2/p$. The slope of each of the final cyclic stress loops βc also decreased with distance. Shear stresses in the soil were induced by the shear interface traction between the pile and the soil and this effect dissipated with increasing distance from the pile. Figure 6b reports the variation of the stress paths for elements E1, E4 and E5 located at the same horizontal distance from the pile (x/D = 0.65) but at different depths (z/L = 0.15, 0.5 and 0.85, respectively). Both the amplitude of the cyclic stress loops and the inclination βc of the stress paths were affected by the depth of the considered elements. Elements E1 and E4 were located above the pile rotation point and were characterised by βc less than 90°.

Element E5 lay below the pile rotation point and it was characterised by an inclination βc of the final stress loop larger than 90°.

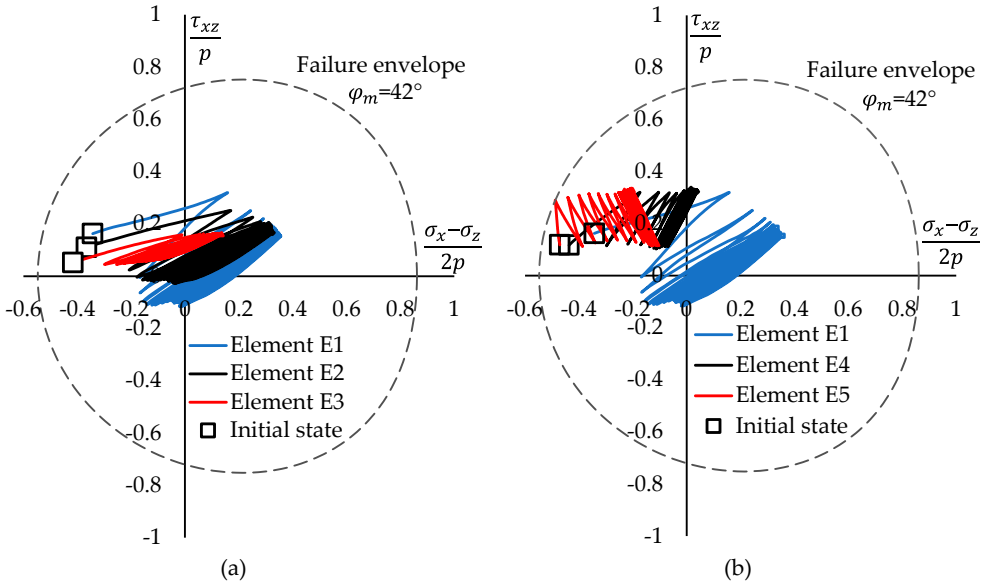

Figure 6. Stress path in the normalised shear stress deviatoric stress plane in terms of (**a**) distance from the pile shaft; (**b**) depth.

The inclination βc versus number of cycles for varying distances and depths are illustrated in Figure 7a,b, respectively. The βc for all elements approached constant state as the cyclic loading proceeds. The relationship between the inclination βc of the final stress cycles and the location of the inspected soil element is reported in Figure 7c for varying distances and in Figure 7d for varying depths. The depth of the soil element had a more pronounced effect on stress path if compared with the distance from the pile.

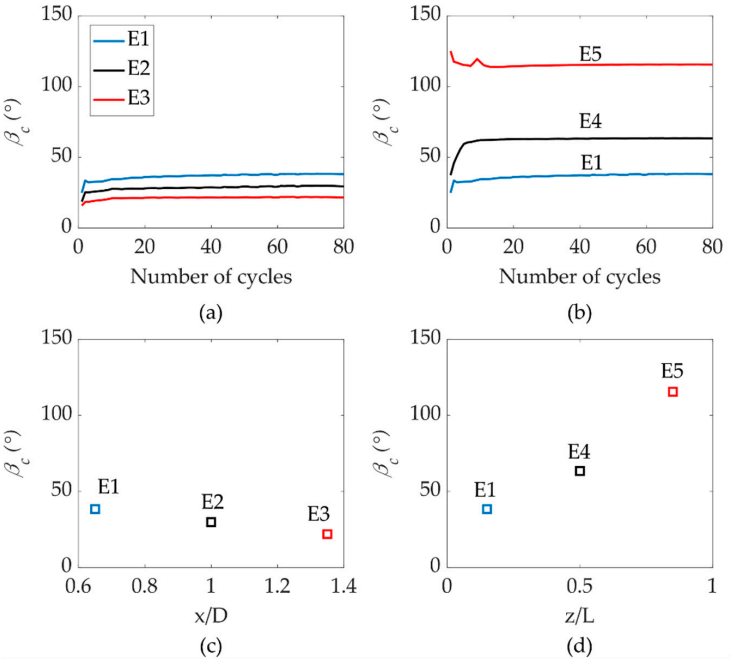

Figure 7. (**a**) Inclination βc versus no. of cycles for varying distances; (**b**) inclination βc versus no. of cycles for varying depths; (**c**) relationship between inclination βc of last stress cycle and distances; (**d**) relationship between inclination βc of last stress cycle and depths.

3. Investigation through Element Testing

3.1. Hollow Cylinder Testing and Stress Notation

The aim of this section was to apply, in laboratory element testing, the stress paths which mimic those determined using the FE analysis and to assess the impact on the observed soil behaviour. For this assessment, the stress paths determined through the FE were simulated in the HCTA, which possesses four degrees of freedom. As highlighted in Section 2, a clear outcome from the FE analysis was the occurrence of simultaneous variation of both normal and shear stresses within the inspected elements. Therefore, this experimental assessment focused on investigating the effect of applying such complex stress paths to a soil element.

In order to facilitate the comparison between the stress paths determined in FE and those applied in the HCTA, the stress notation presented in Figure 8 was adopted in these experiments. A 90° rotation between the reference stress system of the FE and the HCTA was applied as shown in Figure 8: the stress σ_x aligned with the lateral pile load (horizontal) in FE became the axial stress in a HCTA sample, as shown in Figure 8, while the vertical stress σ_z in the FE model became the circumferential stress in the HCTA sample.

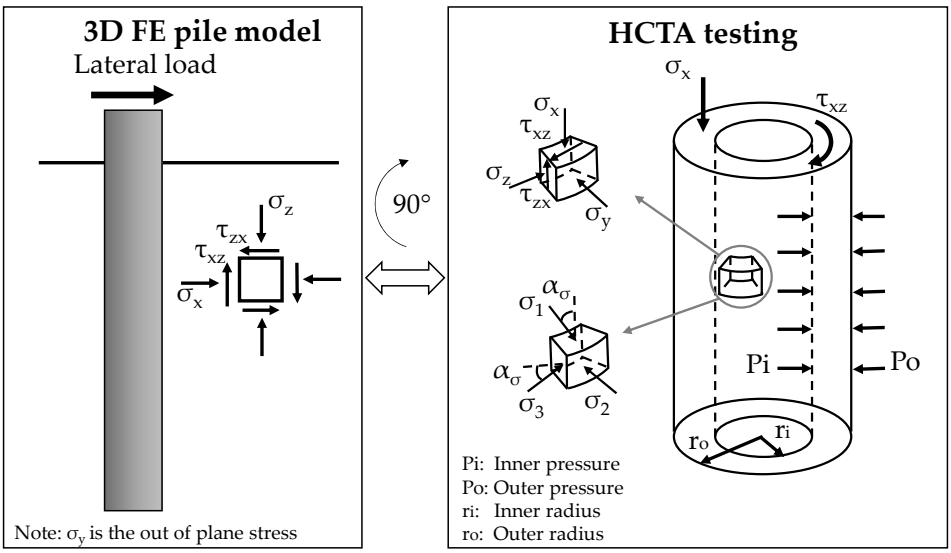

Figure 8. Simplified relationship between reference stress system in the finite element (FE) model and in hollow-cylinder torsional apparatus (HCTA).

In HCTA testing, the capability of controlling independently four stress components came at the expense of variation of the stresses within the sample and average stress quantities needed to be used. In this research, the equations for the calculation of the average stresses (radial stress σ_y and circumferential stress σ_z) follow Hight et al. [29]. Corrections due to the membrane's resistances to the applied axial, radial and shear stress were accounted for using the method suggested by Tatsuoka et al. [30]. However, as the volume changes due to membrane penetration were found to be negligible, no correction was applied.

For the following analysis of the experimental data, the stress state of soil elements is also represented in terms of the mean stress, p, and the generalised deviatoric component of stress, q defined in Equations (1) and (2):

$$p = \frac{\sigma_x + \sigma_z + \sigma_y}{3} = \frac{\sigma_1 + \sigma_2 + \sigma_3}{3}, \quad (1)$$

$$q = \sqrt{\frac{(\sigma_z - \sigma_x)^2 + (\sigma_x - \sigma_y)^2 + (\sigma_y - \sigma_z)^2}{2} + 3\tau_{xz}{}^2}, \quad (2)$$

where σ_1, σ_2, and σ_3 are the major, intermediate and minor principal stresses, respectively. The angle between the major principal stress direction and the vertical x-axes in the HCTA, α_σ, is defined as:

$$\alpha_\sigma = \frac{1}{2}\, tan^{-1}\left(\frac{2\tau_{xz}}{\sigma_x - \sigma_z}\right), \tag{3}$$

Volumetric and deviatoric strain components are also defined in the usual way:

$$\varepsilon_v = \varepsilon_x + \varepsilon_y + \varepsilon_z, \tag{4}$$

$$\varepsilon_q = \frac{\sqrt{2}}{3}\sqrt{(\varepsilon_x - \varepsilon_y)^2 + (\varepsilon_y - \varepsilon_z)^2 + (\varepsilon_z - \varepsilon_x)^2 + \frac{3}{2}\gamma_{xz}^2}, \tag{5}$$

3.2. Material and Specimen Preparation

The experimental testing was conducted at the University of Bristol on Hostun RF (S28) sand, widely characterised in previous studies (i.e., Escribano et al. [31]; Mandolini et al. [11]). This sand is a standard European material for laboratory testing with a high siliceous content (SiO_2) of 98%, angular to subangular grains [32], mean grain size, D_{50} = 0.38 mm, coefficient of uniformity, Cu = D_{60}/D_{10} = 1.9 and coefficient of gradation Cg = $(D_{30})^2/(D_{10}D_{60})$ = 0.97. Its maximum and minimum void ratios are e_{max} = 1.00, e_{min} = 0.62, respectively, while its specific gravity is Gs = 2.65.

The dimensions of hollow cylinder-shaped samples (Figure 8) were: outside radius (r_o) of 50 mm, inner radius (r_i) of 30 mm and height (H) of 200 mm. The HCTA samples were fabricated by dry deposition through the use of a funnel ensuring zero height fall. Following the sand deposition, the sample mould was subjected to a vertically dominated vibration imposed by a shaker under a frequency of about 50 Hz and acceleration of 2 g, under a constant light soil surcharge of 2.8 kPa provided by a vertically guided hollow circular top cap. Once the target density was achieved, the sample was sealed and subjected to a 20 kPa vacuum pressure prior to the removal of the mould. The sample was then transferred inside the HCTA and saturated using CO_2 together with de-aired water and back pressure up to 300 kPa applied. Values of B (Skempton coefficient) [33] of at least 0.97 were systematically measured. Further details of the sample fabrication procedure can be found in Mandolini [28].

3.3. Testing Programme

Three hollow-cylinder torsional tests were carried out, as schematically shown in Figure 9, while the applied stress conditions and initial void ratio prior to isotropic consolidation (e_0) are given in Table 2. Considering the observed progressive evolution towards an asymptotic stress state for all inspected elements, these tests tried to simulate the final asymptotic stress cycles, characterised by an inclination βc with respect of this horizontal stress axes.

All the HCTA samples were firstly isotropically consolidated under the confining stress of 50 kPa (Point A in Figure 9) and then anisotropic stress conditions were reached by applying an additional deviatoric axial stress of 50 kPa (Point B in Figure 9) to simulate the intercept of the observed stress paths with the $(\sigma_x - \sigma_z)/2/p$. From point B, the samples were subjected to about 30,000 stress cycles at different inclination βc with a loading frequency of 0.1 Hz. In order to be able to directly compare the results of the three tests, the cyclic amplitude was chosen such that the larger mobilised friction angle during cyclic loading was similar for all tests. A maximum mobilised friction angle $\varphi_m = 28^\circ$ (which is about 75% of the ultimate friction angle for this material), determined using the Matsuoka-Nakai multiaxial failure criterion, was targeted.

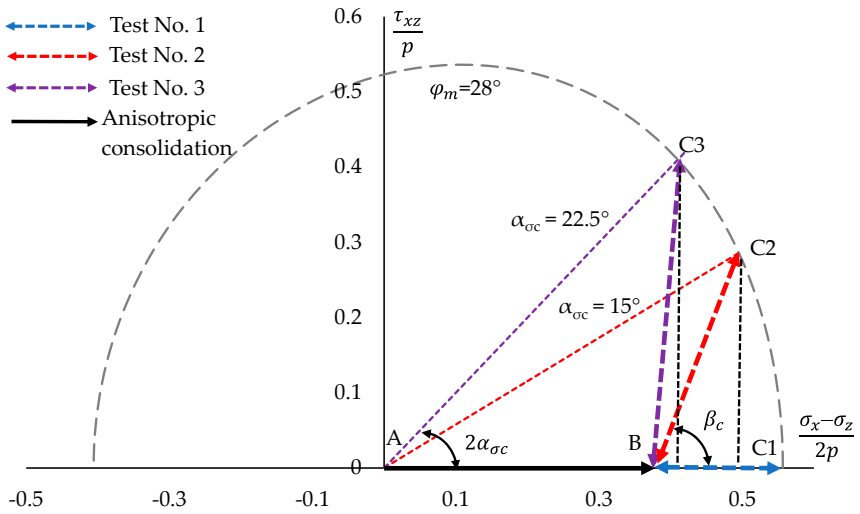

Figure 9. Schematic representation of stress paths imposed in the HCTA tests.

Table 2. List and details of performed hollow-cylinder torsional tests.

Test No.	Stress Path	e_0	$\Delta\sigma_x$ (kPa)	$\Delta\tau_{xz}$ (kPa)	φ_m (°)	$\alpha_{\sigma c}$(°)	β_c(°)	No. Cycles
1	ABC1	0.83	35	0	28	0	0	30,000
2	ABC2	0.80	21	20.5		15	63	30,000
3	ABC3	0.798	7	28.5		22.5	83	26,700

Test 1 considered only the application of normal stress cycles $\Delta\sigma_x$ = 35 kPa (Point C1 in Figure 9). Conversely, Test 2 simulated the additional effect of torsional stress cycles: the sample was subjected to the same cyclic normal stress amplitude $\Delta\sigma_x$ = 21 kPa and an additional cyclic shear stress amplitude $\Delta\tau_{xz}$ = 20.5 kPa (Point C2 in Figure 9), both simultaneously applied. This imposed a cyclic rotation of principal stress axes, $\alpha_{\sigma c}$, varying between 0° and 15°, and it corresponded to an inclination of the stress path βc = 63°, which is consistent with the cyclic loading directions observed by the FE analysis. The maximum rotation of principal stress axes imposed during this cyclic test is indicated by $\alpha_{\sigma c}$ in Figure 9. It should be noted that the rotation of principal stress direction $\alpha_{\sigma c}$ is half of the angle formed by the stress path with the horizontal axes.

Test 3 also simulated the additional effect of torsional stress cycles by imposing $\Delta\sigma_x$ = 7 kPa and $\Delta\tau_{xz}$ = 28.5 kPa (Point C3 in Figure 9) to achieve a maximum rotation of the principal axes $\alpha_{\sigma c}$ of 22.5°. This corresponded to an inclination of the stress path βc = 83°, as shown in Figure 9.

3.4. Experimental Results

The observed deviatoric stress (q) versus deviatoric strain (ε_q) for all the three tests is reported in Figure 10. The three tests follow the same stress path from point A to B, which represents the transition from the initial isotropic stress to the precyclic anisotropic stress condition. From point B, the stress paths applied in the three tests become different. The application of inclined stress paths in the τ_{xz}/p versus $(\sigma_x - \sigma_z)/2/p$ results in a slightly larger maximum applied deviatoric stress despite the same maximum mobilised friction angle. It is also clear that the application of stress paths involving reorientation of the principal stress axes induce a larger development of plastic strain, both in the first and the following cycles. As expected, the plastic deformations accumulated in the first cycle are much larger than those in the consecutive cycles. As the cyclic loading progresses, a gradual sand stiffening occurs in combination with reduced plastic dissipation. The soil response seems to progressively transition from ratcheting to shakedown. Figure 11 reports the trend of accumulated deviatoric strain versus number of cycles for the three tests. While

the mobilised friction angles φ_m in all three tests were similar, a remarkable change in the amount of accumulated deviatoric strain can be observed among the tests.

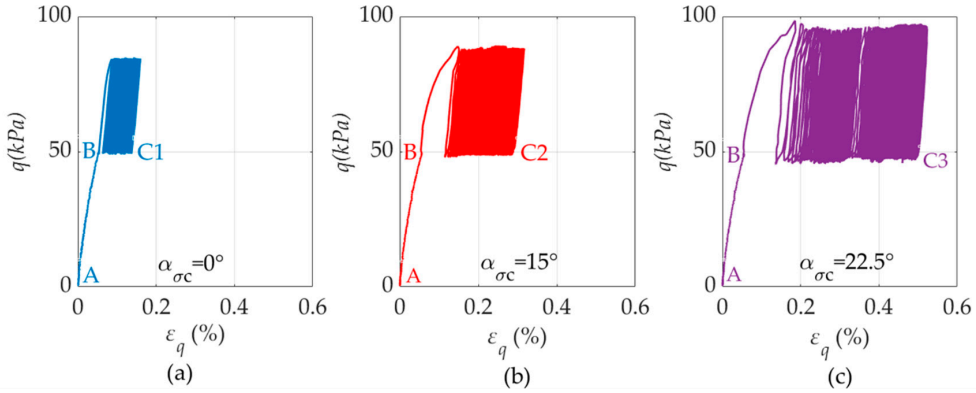

Figure 10. Deviatoric stress versus deviatoric strain trends for (**a**) Test 1, $\alpha_{\sigma c}$ = 0°; (**b**) Test 2, $\alpha_{\sigma c}$ = 15°; and (**c**) Test 3, $\alpha_{\sigma c}$ = 22.5°.

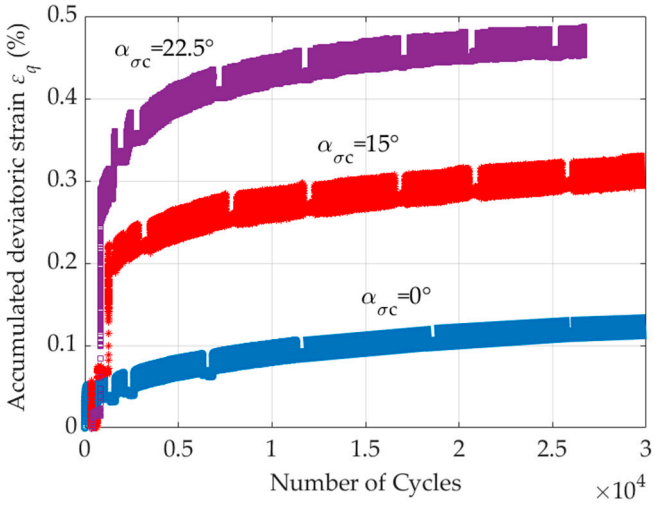

Figure 11. Evolution of deviatoric strain versus number of cycles for the three tests.

The analysis of the accumulation of the main strain components, axial strain (ε_x) and torsional strain (γ_{xz}), during the application of the cycles is presented in Figure 12. For all tests and both strain types, the accumulation was nonlinear with a more pronounced accumulation rate at the start of the cyclic loading and approaching a steady rate at large number of cycles.

Figure 12a shows that the amount of permanent axial deformations increases with the applied rotation of principal stress axes despite the lower amplitude of the axial stress loop. The amplitude of recoverable variation of ε_x within a single cycle appears to diminish with the decrease of the applied cyclic axial stress amplitude. However, the progressive accumulation of permanent axial deformations had an opposite trend, and it increased with higher cyclic torsional stress amplitudes. This suggests that there was an important coupling between cyclic torsional stresses and accumulated axial strains which should be considered when modelling pile–soil interaction problems, as it may affect the evolution of the strain field around the pile and, in turn, its displacement and rotation. Conversely, the axial stress does not seem to have influenced the accumulation of torsional strains (Figure 12b). This coupling is expected to be related to the shear stress–dilatancy relationship, which links shearing to plastic volumetric (and thus axial) deformation and should be properly captured during the application of long-term cyclic loading.

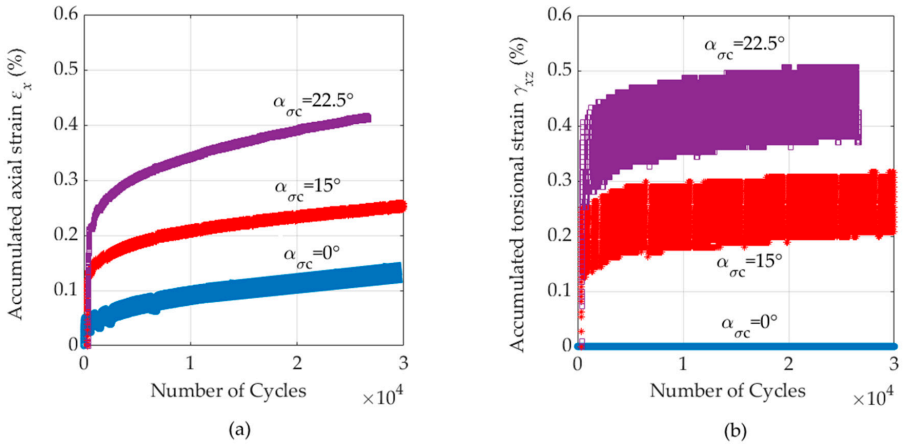

Figure 12. Strain accumulation curves in terms of (**a**) axial strain and (**b**) torsional strain with varying cyclic directions.

Figure 13 reports the trends of accumulated torsional shear versus axial strains, showing that the application of inclined stress paths in the τ_{xz}/p versus $(\sigma_x - \sigma_z)/2/p$ resulted in inclined trends of accumulation in a similar strain plane. The strain paths for individual cycles demonstrate that the application of torsional stress resulted in negligible elastic (recoverable) variations of axial strains but important development of plastic deformation.

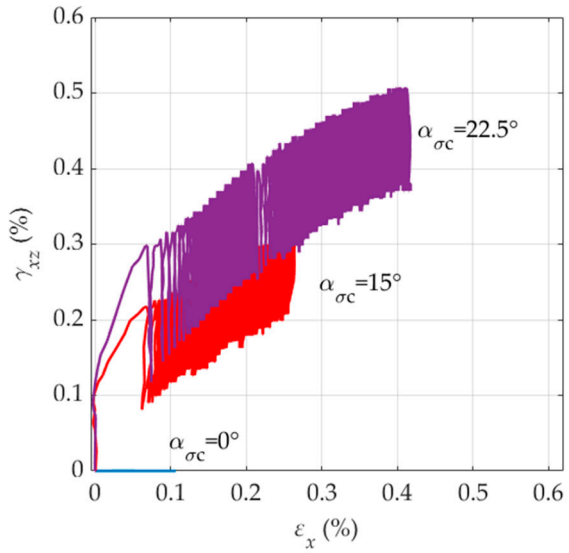

Figure 13. Relationship between torsional strain and axial strain for all three tests.

Figure 14 analyses the relationship between the direction of the accumulated plastic strain $\alpha_{\varepsilon acc}$ and the orientation of principal stress axis for the three tests. The orientation of direction of the accumulated plastic strain $\alpha_{\varepsilon acc}$ is defined as:

$$\alpha_{\varepsilon acc} = \frac{1}{2} tan^{-1}\left(\frac{2\gamma_{xz}}{\varepsilon_{x-\varepsilon_z}}\right), \quad (6)$$

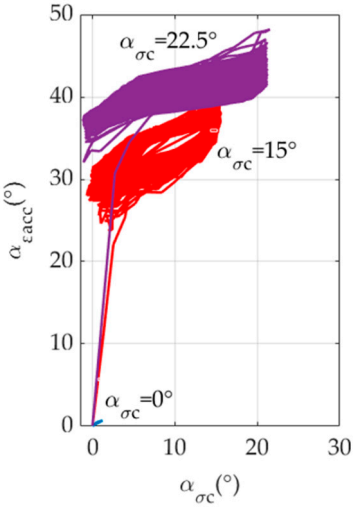

Figure 14. Relationship between orientation of accumulated strain and imposed cyclic reorientation of principal stress axes.

The results show that larger inclinations of accumulated plastic strains were obtained with larger imposed rotation of principal stress axes during cyclic loading. The maximum orientation of plastic strain accumulation was obtained for the first cycle and gradually decreased during the following cycle as ratcheting occurs. It also appears that an asymptotic state was targeted as shakedown conditions were approached.

Overall, these experimental results highlight the importance of considering the reorientation of principal stress axes on the magnitude and direction of strain accumulation. In the context of analysis of cyclic laterally loaded piles, it appears that this feature should be accurately captured by constitutive if reliable predictions of pile performance and pile–soil interaction have to be achieved. In constitutive modelling, improved simulations under the challenging conditions of rotation of principal stress axes may be obtained using the anisotropic critical state theory which was introduced in SANISAND for monotonic loading in the multiaxial stress space [34]. Indeed, appropriate laboratory testing accounting for reorientation of principal stress axes will be also necessary to calibrate such material response.

4. Conclusions

This study employed advanced 3D finite element modelling of a monopile in sand subjected to cyclic lateral loading to investigate the stress paths experienced by surrounding soil elements in order to inform an element laboratory testing program and assess which laboratory procedures closely align with field situations. The 3D finite element model employed the latest developments in cyclic soil constitutive modelling and considered the application of 80 lateral loading cycles. The assessment of the stress paths was limited to soil elements in front of the laterally loaded piles. The FE reveals that a conventional triaxial test was not appropriate to simulate the response of a soil element located in front of the pile. Informed by the 3D finite element model, the laboratory element testing program was carried out using the HCTA, imposing stress paths starting from an initial anisotropic stress state and inducing different reorientations of the principal stress axes. The conclusions of this numerical and experimental work can be summarised as follows:

- The 3D finite element analysis has shown that soil elements in front of the pile undergo complex stress paths involving the cyclic variation of four stress components (three normal stress and one shear stress). The variation of the four stress components is compatible with capability of laboratory testing using the HCTA.
- Analysis of the stress paths in the torsional versus deviatoric stress plane (typically used for HCTA testing) has revealed a quite complex evolution of the stress paths

to reach an asymptotic final cyclic stress condition. The amplitude, location and inclination of the asymptotic stress conditions depends on the location (distance and depth) of the inspected element with respect to the pile.

- The stress path experienced by soil elements in front of cyclic laterally loaded pile may be simulated through cyclic HCTA tests employing stress conditions starting from an initial anisotropic purely deviatoric state and featuring stress cycles characterised by simultaneous variation of axial and torsional stress. This would result in a cyclic reorientation of principal stress axes.
- Comparison of HCTA tests imposing different amounts of cyclic rotation of principal stress axes (including the case of no rotation, typically of conventional triaxial testing) has revealed an important influence of this rotation on the magnitude and direction of accumulated plastic strains.
- In the context of analysis of cyclic laterally loaded piles, it appears that the accurate prediction of magnitude and direction of accumulated plastic strains is necessary to achieve a reliable estimate of the pile–soil interaction mechanism and pile performances. This will require both a constitutive model able to capture such features as well as its calibration with appropriate laboratory soil testing to account for the effect of rotation of the principal stress axes.

Author Contributions: Conceptualization, A.D. and E.I.; formal analysis, X.C. and A.D.; investigation, X.C.; resources, A.D. and E.I.; writing—original draft preparation, X.C.; writing—review and editing, X.C., A.D., E.I., F.P. and H.L.; supervision, A.D. and E.I. All authors have read and agreed to the published version of the manuscript.

Funding: This research received no external funding.

Institutional Review Board Statement: Not applicable.

Informed Consent Statement: Not applicable.

Data Availability Statement: Not applicable.

Acknowledgments: The authors would like to acknowledge the financial support of the first Author from China Scholarship Council (CSC) and University of Bristol.

Conflicts of Interest: The authors declare no conflict of interest.

References

1. Ramírez, L.; Fraile, D.; Brindley, G. *Offshore Wind in Europe: Key Trends and Statistics 2019*; WindEurope: Brussels, Belgium, 2020.
2. Burd, H.J.; Taborda, D.M.; Zdravković, L.; Abadie, C.N.; Byrne, B.W.; Houlsby, G.T.; Gavin, K.G.; Igoe, D.J.; Jardine, R.J.; Martin, C.M.; et al. PISA design model for monopiles for offshore wind turbines: Application to a marine sand. *Géotechnique* **2020**, *70*, 1048–1066. [CrossRef]
3. Byrne, B.W.; Houlsby, G.T.; Burd, H.J.; Gavin, K.G.; Igoe, D.J.; Jardine, R.J.; Martin, C.M.; McAdam, R.A.; Potts, D.M.; Taborda, D.M.; et al. PISA design model for monopiles for offshore wind turbines: Application to a stiff glacial clay till. *Géotechnique* **2020**, *70*, 1030–1047. [CrossRef]
4. Randolph, M.F.; Houlsby, G.T. The limiting pressure on a circular pile loaded laterally in cohesive soil. *Geotechnique* **1984**, *34*, 613–623. [CrossRef]
5. Fan, C.-C.; Long, J.H. Assessment of existing methods for predicting soil response of laterally loaded piles in sand. *Comput. Geotech.* **2005**, *32*, 274–289. [CrossRef]
6. Won, J.Y.; Suroor, H.; Jang, S.; Seo, H. Strain ε50 and stiffness ratio (E50/Su) for Gulf of Mexico clays. In *Frontiers in Offshore Geotechnics, III: Proceedings of the 3rd International Symposium on Frontiers in Offshore Geotechnics (ISFOG 2015), Oslo, Norway, 10–12 June 2015*; CRC Press: Boca Raton, FL, USA, 2015; Volume 1, pp. 1121–1126.
7. Ahmed, S.S.; Hawlader, B. Numerical analysis of large-diameter monopiles in dense sand supporting offshore wind turbines. *Int. J. Geomech.* **2016**, *16*, 04016018. [CrossRef]
8. Andersen, K.H.; Puech, A.A.; Jardine, R.J. Cyclic resistant geotechnical design and parameter selection for offshore engineering and other applications. In *Design for Cyclic Loading: Piles and Other Foundations, Proceedings of the TC-209 Workshop, Paris, France, 4 September 2013*; Presses des Ponts: Paris, France, 2013; pp. 9–44.
9. Wichtmann, T.; Niemunis, A.; Triantafyllidis, T. On the influence of the polarization and the shape of the strain loop on strain accumulation in sand under high-cyclic loading. *Soil Dyn. Earthq. Eng.* **2007**, *27*, 14–28. [CrossRef]

10. Tong, Z.X.; Zhang, J.M.; Yu, Y.L.; Zhang, G. Drained deformation 635 behavior of anisotropic sands during cyclic rotation of principal stress axes. *J. Geotech. Geoenviron. Eng.* **2010**, *136*, 1509–1518. [CrossRef]
11. Mandolini, A.; Diambra, A.; Ibraim, E. Stiffness of granular soils under long-term multiaxial cyclic loading. *Géotechnique* **2020**, 1–17. [CrossRef]
12. Liu, H.Y.; Abell, J.A.; Diambra, A.; Pisanò, F. Modelling the cyclic ratcheting of sands through memory-enhanced bounding surface plasticity. *Géotechnique* **2019**, *69*, 783–800. [CrossRef]
13. Corti, R.; Diambra, A.; Wood, D.M.; Escribano, D.E.; Nash, D.F. Memory surface hardening model for granular soils under repeated loading conditions. *J. Eng. Mech.* **2016**, *142*, 04016102. [CrossRef]
14. Kementzetzidis, E.; Corciulo, S.; Versteijlen, W.G.; Pisanò, F. Geotechnical aspects of offshore wind turbine dynamics from 3D non-linear soil-structure simulations. *Soil Dyn. Earthq. Eng.* **2019**, *120*, 181–199. [CrossRef]
15. Mckenna, F.T. Object-Oriented Finite Element Programming: Frameworks For Analysis, Algorithms And Parallel Computing. Ph.D. Thesis, University of California, Berkeley, CA, USA, 1997.
16. McGann, C.R.; Arduino, P.; Mackenzie-Helnwein, P. A stabilized single-point finite element formulation for three-dimensional dynamic analysis of saturated soils. *Comput. Geotech.* **2015**, *66*, 126–141. [CrossRef]
17. Griffiths, D.V. Numerical modeling of interfaces using conventional finite elements. In Proceedings of the 5th International Conference on Numerical Methods in Geomechanics, Nagoya, Japan, 1–5 April 1985; pp. 837–844.
18. Dafalias, Y.F.; Manzari, M.T. Simple plasticity sand model accounting for fabric change effects. *J. Eng. Mech.* **2004**, *130*, 622–634. [CrossRef]
19. Fan, S.; Bienen, B.; Randolph, M.F. Centrifuge study on effect of installation method on lateral response of monopiles in sand. *Int. J. Phys. Model. Geotech.* **2019**, 1–13. [CrossRef]
20. Heins, E.; Bienen, B.; Randolph, M.F.; Grabe, J. Effect of installation method on static and dynamic load test response for piles in sand. *Int. J. Phys. Model. Geotech.* **2020**, *20*, 1–23. [CrossRef]
21. Staubach, P.; Machaček, J.; Moscoso, M.C.; Wichtmann, T. Impact of the installation on the long-term cyclic behaviour of piles in sand: A numerical study. *Soil Dyn. Earthq. Eng.* **2020**, *138*, 106223. [CrossRef]
22. LeBlanc, C.; Houlsby, G.T.; Byrne, B.W. Response of stiff piles in sand to long-term cyclic lateral loading. *Géotechnique* **2010**, *60*, 79–90. [CrossRef]
23. Roesen, H.R.; Ibsen, L.B.; Andersen, L.V. Experimental testing of monopiles in sand subjected to one-way long-term cyclic lateral loading. In Proceedings of the 18th International Conference on Soil Mechanics and Geotechnical Engineering, Paris, France, 2–6 September 2013; pp. 2391–2394.
24. Liu, H.Y.; Diambra, A.; Abell, J.A.; Pisanò, F. Memory-Enhanced plasticity modeling of sand behavior under undrained cyclic loading. *J. Geotech. Geoenviron. Eng.* **2020**, *146*, 04020122. [CrossRef]
25. Corti, R.; Gourvenec, S.M.; Randolph, M.F.; Diambra, A. Application of a memory surface model to predict whole-life settlements of a sliding foundation. *Comput. Geotech.* **2017**, *88*, 152–163. [CrossRef]
26. Ishihara, K.; Towhata, I. Sand response to cyclic rotation of principal stress directions as induced by wave loads. *Soils Found.* **1983**, *23*, 11–26. [CrossRef]
27. Matsuoka, H.; Nakai, T. Stress-Deformation and strength characteristics of soil under three different principal stresses. *Proc. JSCE* **1974**, 59–70. [CrossRef]
28. Mandolini, A.; Diambra, A.; Ibraim, E. Strength anisotropy of fibre-reinforced sands under multiaxial loading. *Géotechnique* **2019**, *69*, 203–216. [CrossRef]
29. Hight, D.W.; Gens, A.; Symes, M.J. The development of a new hollow cylinder apparatus for investigating the effects of principal stress rotation in soils. *Géotechnique* **1983**, *33*, 355–383. [CrossRef]
30. Tatsuoka, F.; Sonoda, S.; Hara, K.; Fukushima, S.; Pradhan, T.B. Failure and deformation of sand in torsional shear. *Soils Found.* **1986**, *26*, 79–97. [CrossRef]
31. Escribano, D.E.; Nash, D.F.; Diambra, A. Local and global volumetric strain comparison in sand specimens subjected to drained cyclic and monotonic triaxial compression loading. *Geotech. Test. J.* **2018**, *42*, 1006–1030. [CrossRef]
32. Ibraim, E.; Diambra, A.; Russell, A.R.; Wood, D.M. Assessment of laboratory sample preparation for fibre reinforced sands. *Geotext. Geomembr.* **2012**, *34*, 69–79. [CrossRef]
33. Skempton, A.W. The pore-pressure coefficients A and B. *Géotechnique* **1954**, *4*, 143–147. [CrossRef]
34. Petalas, A.L.; Dafalias, Y.F.; Papadimitriou, A.G. SANISAND-F: Sand constitutive model with evolving fabric anisotropy. *Int. J. Solids Struct.* **2020**, *188*, 12–31. [CrossRef]